



**HAL**  
open science

## Extrusion-Spheronization of UiO-66 and UiO-66\_NH<sub>2</sub> into Robust-Shaped Solids and Their Use for Gaseous Molecular Iodine, Xenon, and Krypton Adsorption

Alla Abramova, Nelly Couzon, Maeva Leloire, Philippe Nerisson, Laurent Cantrel, Sébastien Royer, Thierry Loiseau, Christophe Volkringer, Jérémy Dhainaut

### ► To cite this version:

Alla Abramova, Nelly Couzon, Maeva Leloire, Philippe Nerisson, Laurent Cantrel, et al.. Extrusion-Spheronization of UiO-66 and UiO-66\_NH<sub>2</sub> into Robust-Shaped Solids and Their Use for Gaseous Molecular Iodine, Xenon, and Krypton Adsorption. ACS Applied Materials & Interfaces, 2022, ACS Applied Materials & Interfaces, 14 (8), pp.10669-10680. 10.1021/acsami.1c21380 . hal-03588293

**HAL Id: hal-03588293**

**<https://hal.univ-lille.fr/hal-03588293v1>**

Submitted on 3 May 2022

**HAL** is a multi-disciplinary open access archive for the deposit and dissemination of scientific research documents, whether they are published or not. The documents may come from teaching and research institutions in France or abroad, or from public or private research centers.

L'archive ouverte pluridisciplinaire **HAL**, est destinée au dépôt et à la diffusion de documents scientifiques de niveau recherche, publiés ou non, émanant des établissements d'enseignement et de recherche français ou étrangers, des laboratoires publics ou privés.

1 Extrusion-Spheronization of UiO-66 and UiO-  
2 66\_NH<sub>2</sub> into Robust Shaped Solids and their Use for  
3 Gaseous Molecular Iodine, Xenon and Krypton  
4 Adsorption

5 *Alla Abramova<sup>a</sup>, Nelly Couzon<sup>b</sup>, Maëva Leloire<sup>b,c</sup>, Philippe Nerisson<sup>c</sup>, Laurent Cantrel<sup>c</sup>, Sébastien*  
6 *Royer<sup>b</sup>, Thierry Loiseau<sup>b</sup>, Christophe Volkringer<sup>b</sup>, Jérémy Dhainaut<sup>b,\*</sup>*

7

8 <sup>a</sup> Univ. Lille, CNRS, INRA, Centrale Lille, Univ. Artois, FR 2638 – IMEC – Institut Michel-  
9 Eugène Chevreul, F-59000 Lille, France.

10 <sup>b</sup> Univ. Lille, CNRS, Centrale Lille, Univ. Artois, UMR 8181 - UCCS - Unité de Catalyse et  
11 Chimie du Solide, F-59000 Lille, France.

12 <sup>c</sup> Institut de Radioprotection et de Sûreté Nucléaire (IRSN), PSN-RES/SEREX, Saint-Paul Lez  
13 Durance, 13115, France.

14

15 Keywords: Metal-Organic Frameworks ; Extrusion-spheronization ; Shaping ; Iodine Capture ;

16 Xe/Kr separation

1  
2  
3  
4  
5  
6  
7  
8  
9  
10  
11  
12  
13  
14  
15  
16  
17  
18  
19

**ABSTRACT.**

The use of an extrusion-spheronization process was investigated in order to prepare robust and highly-porous extrudates and granules starting from UiO-66 and UiO-66\_NH<sub>2</sub> metal-organic framework powders. As-produced materials were applied to the capture of gaseous iodine, and the adsorption of xenon and krypton. In this contribution, biosourced chitosan and hydroxyethyl cellulose (HEC) are used as binders, added in low amounts (less than 5 wt% of the dried solids), as well as a colloidal silica as a co-binder when required. Characterizations of the final shaped materials reveal that most physico-chemical properties are retained, excepted the textural properties which are impacted by the process and the proportion of binders (BET surface area reduction from 5 to 33 %). On the other hand, the mechanical resistance of the shaped materials toward compression is greatly improved by the binders presence and their respective contents, from 0.5 N for binderless UiO-66 granules to 17 N for UiO-66@HEC granules. UiO-66\_NH<sub>2</sub>-based granules demonstrated consequent iodine capture after 48 hours, up to 527 mg/g, in line with the pristine UiO-66\_NH<sub>2</sub> powder (565 mg/g) and proportionally to the retaining BET surface area (-5 % after shaping). Analogously, the shaped materials presented xenon and krypton sorption isotherms correlated to their BET surface area and high predicted xenon/krypton selectivity, from 7.1 to 9.0. Therefore, binder-aided extrusion-spheronization is an adapted method to produce shaped solids with adequate mechanical resistance and retained functional properties.

1  
2  
3  
4  
5  
6  
7  
8  
9  
10  
11  
12  
13  
14  
15  
16  
17  
18  
19  
20  
21  
22  
23

## INTRODUCTION

Currently, the nuclear industry provides about 10 % of the world electricity through 445 power reactors, making it the fourth source of electricity production behind coal (38 %), natural gas (23 %), and hydroelectricity (16 %). While the number of power plants remained somehow constant since 1996, about 50 new reactors are under construction. Recently, the European Commission declared nuclear energy as sustainable. Hence, a consequent research and development effort is devoted to the continuous improvement of the power reactors safety, the sustainability of the electricity production, and the long-term waste management. Besides, novel solutions to valorise fission products or to limit the effects of potential nuclear plant accidents are desirable.

For instance, in the case of a nuclear meltdown, as occurred in 2011 at Fukushima Daiichi nuclear power plant, venting should be done to avoid containment overpressurisation,<sup>1</sup> which could cause irremediable structural damage and further release of radioactive material with widespread effects – as it happened.<sup>2</sup> However, the vented steam contains a significant concentration of volatile radionuclides and especially iodine-131 which is a major radionuclide comprising about 3 wt.% of the total fission products from uranium neutron reactions.<sup>1</sup> Importantly, <sup>131</sup>I released in the environment can be either inhaled or ingested through food products (vegetables, dairy farms, etc.) and penetrate the thyroid tissues, increasing the incidence of thyroid cancers as observed following the Chernobyl disaster.<sup>3</sup>

In order to minimize the release of radionuclides, and hence their consequences on the health and the environment, passive filtration systems have been developed by the nuclear industry to treat the vented contaminated steam. Especially, Filtered Containment Venting Systems (FCVS), either based on the use of a scrubber (wet FCVS) or solid filter (dry FCVS), allow to trap

1 above 99 % of molecular iodine but are much less efficient for organic iodide species.<sup>1,4</sup> The cap-  
2 ture of these organics can be performed by using a fixed bed of silver-doped zeolites, which is  
3 typically installed downstream of the first filtration step.<sup>4</sup> For instance, up to 455 mg of molecular  
4 iodine can be captured with a gram of silver-doped ZSM-5 zeolite.<sup>5</sup> However, the zeolite trapping  
5 capacities with respect to iodine derivatives such as CH<sub>3</sub>I may be inhibited by gaseous contami-  
6 nants (mainly CO).<sup>6</sup> Thus, to further improve the FCVS efficiency, an alternative approach can be  
7 to study the trapping properties of innovative porous material with similar or higher adsorption  
8 capacities toward iodine species and exhibiting larger pores.<sup>7</sup> Of note, the material should be stable  
9 at 140 °C under steam and irradiation, related to the typical conditions occurring in a vented con-  
10 taminated steam.<sup>8</sup> Activated carbons impregnated with tri-ethylene-di-amine (TEDA) have been  
11 applied for I<sub>2</sub> and CH<sub>3</sub>I capture. They present long-term performance under simulated operating  
12 conditions, with up to 99 % of the CH<sub>3</sub>I retained after 15 months.<sup>9</sup> However, they exhibit a low  
13 autoignition temperature which makes them unsafe to use in the nuclear field.<sup>7</sup> Metal-Organic  
14 Frameworks (MOFs) have been studied from 2011, first using the Zn-based ZIF-8 MOF which  
15 possesses pores size adequate for molecular iodine (I<sub>2</sub>kinetic diameter = 5 Å).<sup>10</sup> A major breakthrough  
16 was reported with MOFs presenting electron donor groups attached to the organic linkers, since  
17 their presence leading to the polarization of the electron cloud of molecular iodine.<sup>11</sup> Iodine load-  
18 ings above 500 mg per gram of MOF can be obtained,<sup>12</sup> with a record uptake of 2.79 g/g.<sup>13</sup>

19 While iodine-131 represents one of the major gaseous fission products, every fission event  
20 also produces 0.25 to 0.30 atom of valorizable noble gas species including xenon and krypton  
21 elements, with Xe atoms being seven times more likely to be produced than Kr atoms.<sup>14</sup> The pro-  
22 cess off-gas containing the noble gas species as well as <sup>129</sup>I, <sup>14</sup>CO<sub>2</sub>, <sup>3</sup>H<sub>2</sub>O, and NO<sub>x</sub> are usually  
23 vented to the atmosphere, which could arise hazardous problematics. On the other hand, xenon is

1 extremely scarce in the Earth's atmosphere (about 87 ppb),<sup>15</sup> making it the most expensive noble  
2 gas to purchase, while it has a number of key applications, especially in the medical, lighting, and  
3 electronic fields. Hence, it is of utmost importance to develop novel ways to capture radioactive  
4 components from the process off-gas and produce high purity Xe gas. In this line, many porous  
5 solids have been applied to the separation of xenon over krypton. Activated carbons present inter-  
6 esting xenon uptakes but low Xe/Kr selectivity, between 2 and 3.<sup>16</sup> Moreover, the presence of NO<sub>x</sub>  
7 in the process off-gas forbids their use due to possible fire hazards. On the other hand, zeolites  
8 show remarkable Xe/Kr selectivity, over 4, but only limited noble gas uptakes.<sup>17</sup> Of note, silver-  
9 doped zeolites gave rise to higher xenon uptakes and Xe/Kr selectivity than their protonated  
10 form.<sup>18</sup> MOFs, presenting some of the highest xenon uptakes and Xe/Kr selectivities,<sup>15</sup> are hence  
11 promising materials for this application. The SBMOF-1 compound is one of the current leading  
12 material for separation, with a Xe/Kr selectivity of 16 owing to its pores closely matching the size  
13 of Xenon atoms.<sup>19</sup> The record for Xenon uptake in a MOF was obtained with the PCN-14 com-  
14 pound, having a Xenon uptake of 7.1 mmol/g, 50 % higher than the best activated carbon.<sup>20</sup>

15 MOFs are hybrid crystalline materials whose structure results from the assembly of metal-  
16 lic nodes (clusters or ions) with multitopic organic linkers through coordination bondings. Their  
17 strength lies in this modular nature, as most of their physico-chemical properties can be tailored  
18 for specific applications. This resulted in the report of over 10.000 MOF structures within the last  
19 20 years, with several prototypal MOFs presenting surface areas ( $S_{\text{BET}}$ ) over 1.000 m<sup>2</sup>/g and pore  
20 sizes up to 98 Å.<sup>21</sup> Owing to these properties, selected MOFs demonstrate excellent performances  
21 in adsorption, catalysis and separation applications.<sup>21</sup> On the downside, their structure is rarely

1 stable above 300 °C in air (thermal decomposition) or in aqueous phase (hydrolysis of the coordi-  
2 nation bonds).<sup>22</sup> For commercial applications, MOF structures based on trivalent metals or above,  
3 less prone to hydrolysis, should be preferred.

4 The  $[Zr_6O_4(OH)_4(O_2C-C_6H_4-CO_2)_6]$  MOF structural archetype, also known as UiO-66, has  
5 been widely investigated owing to its good stability against moisture, related to the coordination  
6 of hexanuclear  $Zr_6O_4(OH)_4$  clusters with up to 12 terephthalate linkers, and high adsorption capac-  
7 ity, in line with its BET surface area exceeding 1.000 m<sup>2</sup>/g.<sup>23</sup> Moreover, the UiO-66 MOF presents  
8 a pore size distribution typically between 8 and 11 Å, due to the presence of defects in its struc-  
9 ture.<sup>23</sup> Starting from the structural archetype, several sub-structures can be obtained, either by  
10 changing the metal (Hf, Ce, Th, U, Np etc.) or the organic linker (fumarate: UiO-66-FA, bi-  
11 phenyldicarboxylate: UiO-67, etc.), or even by adding organic functionalities to the terephthalate  
12 linkers (UiO-66\_NH<sub>2</sub>, UiO-66\_OH, UiO-66\_COOH etc.).<sup>24-27</sup>

13 Owing to their good stability and scalable synthesis, this family of MOFs has been used  
14 for the capture of a broad array of molecules in gas and liquid phases,<sup>28</sup> including I<sub>2</sub>.<sup>29</sup> In particular,  
15 UiO-66\_NH<sub>2</sub> has been applied for the capture of substantial amounts of NO<sub>2</sub>,<sup>30</sup> HCl and Cl<sub>2</sub>,<sup>31</sup> and  
16 CO<sub>2</sub>,<sup>32</sup> owing to their high binding energy with the electro-donor amino groups. Recently, our  
17 group applied this MOF for the immobilization of <sup>131</sup>I-iodine under simulated nuclear accidental  
18 conditions.<sup>8</sup> UiO-66\_NH<sub>2</sub> millimetric granules were preloaded with 7.8 mg of <sup>131</sup>I<sub>2</sub> per gram of  
19 MOF and further subjected to a continuous wet air flow with a relative humidity of 25 %, an  
20 absolute pressure of 3.5 bar and a temperature of 120 °C.<sup>8</sup> Moreover, a gamma radiation dose rate  
21 of 1.9 kGy/h was applied. After 30 hours under these severe nuclear accidental conditions, no

1 leakage of  $^{131}\text{I}_2$  was detected and the UiO-66\_NH<sub>2</sub> structure remained intact. Thus, this MOF can-  
2 didate is promising for applications linked to fission products mitigation in a nuclear accident  
3 context.

4         However, one of the limits of this study is the weak mechanical resistance of the binderless  
5 granules used, below 1 Newton. In a fixed bed, the solids are subjected to friction and/or abrasion,  
6 which will produce fine particles in the case of low mechanical resistance, and will clog the filters  
7 typically installed downstream of the fixed bed overtime. This in turn would dangerously arise the  
8 pressure within the installation. More generally, MOFs shaping remains a major bottleneck prior  
9 to their wider use in the everyday life due to several reasons: 1/ MOFs cannot undertake sintering,  
10 which is typically used to reinforce inorganic materials, due to their mild thermal resistance (typ-  
11 ically below 300 °C); 2/ the use of a large amount of binders significantly lower their perfor-  
12 mances, making them less attractive compared to activated carbons and zeolites; and 3/ most MOF  
13 structures are not rigid enough to withstand high compression pressure or shearing force, as  
14 reached when using pelletization, extrusion, or granulation processes.<sup>33</sup> However, it was reported  
15 that the UiO-66-based MOFs offer an adequate resistance for binderless pelletization,<sup>34</sup> but the  
16 resulting pellets are not suited for a fixed bed application due to the resulting spatial heterogenei-  
17 ties. More suited solids for fixed beds include extrudates and granules, giving the best compromise  
18 between pressure drop, contact surface, and filling ratio. UiO-66 and UiO-66\_NH<sub>2</sub> compounds  
19 have been previously shaped under the granules form in the presence of binders,<sup>35-37</sup> allowing to  
20 obtain relatively resistant shaped bodies at the expense of the porosity. Another derivative, UiO-  
21 66\_COOH, has been shaped following extrusion, in the presence of a silicon resin which affected  
22 greatly the resulting porosity ( $S_{\text{BET}} = -40\%$  with 5.5 wt% of silicon resin).<sup>38</sup> Intriguingly, no ex-  
23 trusion of UiO-66 nor UiO-66\_NH<sub>2</sub> has been reported so far.



1 Hence, the following study is devoted to the preparation of robust and highly porous ex-  
2 trudates and granules made of UiO-66 and UiO-66\_NH<sub>2</sub> compounds. For this purpose, a few per-  
3 cents of a biosourced binder, either a derived of cellulose or chitosan, are added to a MOF-based  
4 paste prior to extrusion. The extrudates were characterized as such, or further spheronized to pro-  
5 duce granules. This is the first time that an extrusion-spheronization process is applied to a MOF-  
6 based material. The I<sub>2</sub> adsorption capacity of these granules was evaluated using a specific testing  
7 bench. Notably, chitosan possesses inherent amino functions, which could either improve or at  
8 least milder the effect of the binder presence over the I<sub>2</sub> uptake of the resulting composite. Finally,  
9 Xe and Kr sorption isotherms of these composites were also measured at room temperature to  
10 diversify their possible applications for the nuclear energy field and the valorization of xenon gas.

## 11 **EXPERIMENTAL SECTION**

12 Reagents: *N,N*-Dimethylformamide (DMF, Carlo Erba 99.9 %), methanol (MeOH, VWR  
13 98.5+ %), zirconium tetrachloride (ZrCl<sub>4</sub>, ACROS Organics 98 %), acetic acid (CH<sub>3</sub>COOH, VWR  
14 99+ %), formic acid (HCOOH, ACROS Organics 98 %), terephthalic acid (H<sub>2</sub>BDC, Alfa Aesar  
15 98 %), 2-aminoterephthalic acid (H<sub>2</sub>BDC-NH<sub>2</sub>, Aldrich 99 %), 2-hydroxyethyl cellulose (HEC,  
16 Aldrich M<sub>w</sub> = 1,300,000 g/mol), deacetylated chitin (chitosan, Aldrich M<sub>w</sub> = 310,000 to 375,000  
17 g/mol), Ludox® HS-40 (colloidal silica, Sigma-Aldrich, 40 %), potassium iodide (KI, Alfa Aesar  
18 99 %). All reagents were used without further purification.

19 **Synthesis of UiO-66.** Its preparation was based on the scale-up synthesis protocol described  
20 elsewhere.<sup>5</sup> Briefly, 3 L of DMF, 40 g of ZrCl<sub>4</sub> (+150 mL of DMF for rinsing), 56 g of H<sub>2</sub>BDC  
21 (+100 mL of DMF for rinsing), and 0.65 L of HCOOH were added successively in a mechanically  
22 stirred, 8-L stainless steel autoclave. The latter was sealed, and the starting reactants were mixed

1 at 100 rounds per minute (rpm) for 24 hours at 120 °C. After cooling down the autoclave, the  
2 mixture was collected and the resulting solid was separated from the supernatant by centrifugation  
3 at 4,000 rpm for 10 minutes. The solid was then dispersed twice for 24 hours in fresh DMF and  
4 three times in MeOH, with separation by centrifugation in-between. Finally, the white powdered  
5 product was dried during 1 hour at 100 °C and then 8 hours at 150 °C. Final yield = 65 mol% upon  
6 Zr.

7 **Synthesis of UiO-66\_NH<sub>2</sub>**. A similar protocol was used, with slightly different weights of the  
8 starting chemical reactants but identical reaction conditions. More specifically, 80 g of ZrCl<sub>4</sub> and  
9 120 g of H<sub>2</sub>BDC-NH<sub>2</sub> were added in the 8-L autoclave. Final yield = 85 mol% upon Zr.

10 **Extrusion-spheronization of UiO-66 and UiO-66\_NH<sub>2</sub> solids**. All steps were conducted using a  
11 Caleva Multi Lab apparatus. At first, a MOF-based paste was formed by kneading about 10 g of  
12 powdered MOF (either UiO-66 or UiO-66\_NH<sub>2</sub>) with about 12 g of a gel containing the binder  
13 (either 2-hydroxyethyl cellulose – HEC – or deacetylated chitin – chitosan) at 150 rpm for 30  
14 minutes. When using HEC as a binder with UiO-66 powder, a second batch composition was  
15 obtained by adding 0.47 g of a silica suspension. The exact composition of the pastes as well as  
16 the protocol to prepare gels are given in SI. Successive additions of portions of the MOF powder  
17 gave better paste homogeneity. The paste was recovered, and pushed into the feed zone of a single-  
18 screw extruder rotating at 90 rpm. At the end of the screw, a die with multiple holes of diameter 1  
19 mm was fitted. The as-obtained extrudates (Fig. S1) were dried overnight at 120 °C.

20 For the production of granules, 1.5 g of as-obtained extrudates were directly placed onto  
21 the 3 mm pitch plate of the spheronization module. The plate was rotated at 2,500 rpm for 10

1 minutes. After sieving (mesh size 500  $\mu\text{m}$ ), 1.2 to 1.4 g of rounded granules were obtained. The  
2 granules were also dried overnight at 120  $^{\circ}\text{C}$ .

3 All solids are named according to their MOF structure and the binder used, following the  
4 denomination MOF@binder related to the samples: UiO-66@HEC, UiO-66@chitosan, UiO-  
5 66\_  $\text{NH}_2$ @HEC, UiO-66\_  $\text{NH}_2$ @chitosan, and UiO-66@HEC-Ludox.

6 **Characterization.** Powder X-ray diffraction patterns (XRD) were collected on a Bruker D8  
7 Advanced AXS diffractometer equipped with Cu  $\text{K}_{\alpha 1}$  monochromatic radiation source ( $\lambda = 1.5418$   
8  $\text{\AA}$ ) and operated at 40 kV and 30 mA. X-ray diagrams were recorded within the  $5^{\circ}$ – $50^{\circ}$  region with  
9 a  $0.02^{\circ}$  step size (step time = 0.5 s). Nitrogen sorption isotherms at 77 K were measured with a  
10 Micromeritics Tristar II Plus apparatus. Prior to measurement, the samples were degassed for 8 h  
11 at 150  $^{\circ}\text{C}$ . The surface area ( $S_{\text{BET}}$ ) was determined from applying the multipoint B.E.T. algorithm  
12 over a linear portion at relative pressures in the range 0.04–0.25. The micropore and total pore  
13 volumes were estimated from the adsorbed volume of nitrogen at relative pressures of 0.25 and  
14 0.99, respectively. Scanning electron microscopy (SEM) images were taken using a JEOL JSM  
15 6700F. The solids were directly deposited on a carbon tape and electron conductivity was obtained  
16 by depositing silver lacquer. ImageJ (v.1.52a) was used to determine the crystals size distribution  
17 from SEM micrographs. Thermogravimetric analyses (TGA) were conducted with a Mettler  
18 Toledo TGA/DSC 3+ thermal analyzer over the range 25–600  $^{\circ}\text{C}$  under air flow (80 ml/min),  
19 following a heating rate of 2  $^{\circ}\text{C}\cdot\text{min}^{-1}$ . The Fourier Transform Infrared (FTIR) spectra were  
20 recorded at room temperature between 4000 and 400  $\text{cm}^{-1}$  using a Perkin Elmer Spectrum Two  
21 Spectrometer equipped with an ATR sampling module. The deacetylation degree (DD) of the  
22 commercial chitosan was evaluated following the equation:  $\text{DD} = 1 - (A_{1320}/A_{1420} - 0.3822)/3.133$ .<sup>39</sup>  
23 The averaged bulk density was determined by weighting ten dried extrudates and measuring their

1 dimensions with a digital caliper. Compressive strength of the solids was determined using a Vinci  
2 Technologies Versatile Crushing Strength Tester, using a set of flat anvil and hammer. The load  
3 applied was recorded by the force sensor as a function of the displacement of the punch at a  
4 constant speed of 0.6 mm/min until failure, happening at the ultimate crushing strength of the solid  
5 (called compressive strength hereafter for simplicity). For each sample, ten representative solids  
6 were crushed and the resulting compressive strength values, given in Newton, were averaged.  
7 Xenon and krypton sorption isotherms at  $293.15 \pm 2$  K were measured separately with a  
8 Micromeritics ASAP 2020 PLUS. Prior to measurement, the samples were degassed for 8 h at 120  
9 °C. Xe/Kr selectivity is determined from the ratio of Henry's constants, which are obtained from  
10 the slope of the isotherms in a linear, low-pressure range ( $p/p_0 < 0.03$ ).

11 **Iodine capture test.** The adsorption capacity of the investigated MOF-based granules towards  
12 I<sub>2</sub> was investigated using a dedicated experiment.<sup>12</sup> The experimental setup devoted to I<sub>2</sub> sorption  
13 test can be divided in three main parts: the generation of the I<sub>2</sub> inlet flow, a fixed-bed glass reactor  
14 and the quantification system composed of bubblers containing potassium iodide solution (KI, 0.1  
15 M) and an UV-Vis spectrometer (Figure S2). Gaseous iodine is produced from the sublimation  
16 process (0.2 mg/h) of crystalline iodine beads in a permeation chamber (VICI Metronics Inc.,  
17 Dynacalibrator Model 150) set at 100 °C, and is carried by a controlled flow of argon (10 nL/h ;  
18 [I<sub>2</sub>] = 100 ppm) and then, transferred into the glass sintered cell (4 mm diameter) at room  
19 temperature (20 °C ± 1 °C) through an inert PTFE line.

20 The quantity of iodine passing through the glass sintered cell (*i.e.* not adsorbed by the  
21 granules) is collected in a bubbler held in a 2-L opaque flask of 0.1 M KI solution, leading to the  
22 quantitative formation of the triiodide ion I<sub>3</sub><sup>-</sup>. A peristaltic pump allows the continuous flow of the  
23 solution through the quartz cell of a UV-vis spectrometer and the concentration of I<sub>3</sub><sup>-</sup> generated in

1 the bubbler is measured every 4 minutes at the absorbance of the selected band ( $\lambda_{\max} = 352 \text{ nm}$ ).  
2 The kinetic adsorption of iodine is then calculated from the difference between a blank curve (*i.e.*  
3 no adsorbing material) and the curve collected in the presence of the granules in the reactor. The  
4 content of molecular iodine trapped within the porous framework is then calculated by the means  
5 of a calibration curve.

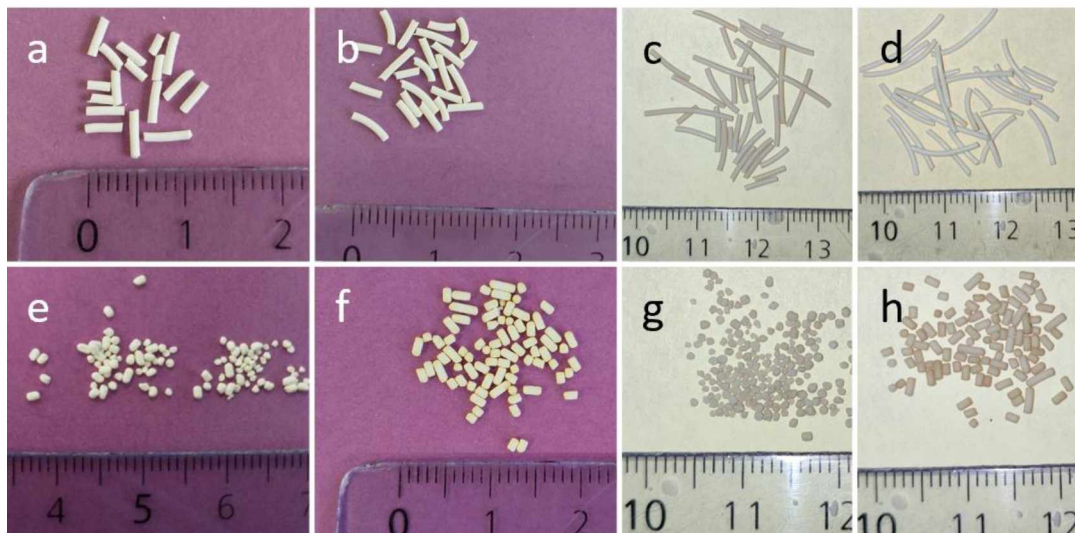
6 Prior to analysis, the MOF-based granules were thermally treated *ex-situ* overnight at 120  
7 °C in order to remove entrapped species within the pores. 20 mg of activated UiO-66-based  
8 materials were transferred into the glass sintered cell, leading to a 1 cm bed height. The estimated  
9 residence time is about 0.04 second.

## 10 **RESULTS AND DISCUSSION**

### 11 **Impact of the shaping over the properties of UiO-66/UiO-66\_NH<sub>2</sub>**

12 After extrusion and spheronization, and as observed on Figure 1 and Figure S1, all shaped  
13 materials are dust-free and their aspect is homogeneous. The diameter of all extrudates and  
14 granules is comprised between 0.89 and 0.96 mm, while the length of the granules seems related  
15 to the resistance of the extrudates towards attrition, and hence to the nature of the binder. Indeed,  
16 starting from extrudates with comparable lengths, UiO-66@chitosan and UiO-66\_NH<sub>2</sub>@chitosan  
17 are spheronized into 1.88 mm and 1.63 mm rounded granules, respectively, while UiO-66@HEC  
18 and UiO-66\_NH<sub>2</sub>@HEC lead to spherical solids (length = 0.9-1.2 mm). Several authors have  
19 shown that the spheronization mechanism,<sup>40</sup> which is based on abrasion, typically includes several  
20 stages: starting from extrudates, cylinders with rounded ends are produced first. Then, dumbbell-  
21 like solids are formed, and are further splitted into ellipsoidal objects. Finally, spheres are obtained.

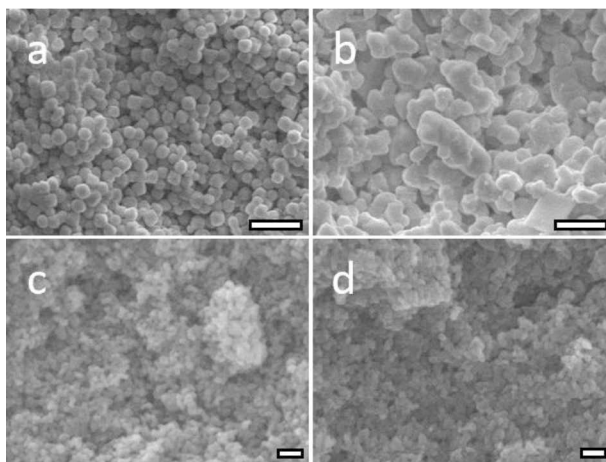
1 Thus, different shapes come from a different stage reached for a similar amount of mechanical  
2 energy provided.



3  
4 **Figure 1.** Photographs of (a-d) extrudates and (e-h) granules of (a, e) UiO-66@HEC, (b, f) UiO-  
5 66@chitosan, (c, g) UiO-66\_NH<sub>2</sub>@HEC, and (d, h) UiO-66\_NH<sub>2</sub>@chitosan.

6 At the microscopic scale, several features can be observed. Notably the initial UiO-66 and  
7 UiO-66\_NH<sub>2</sub> powders, prepared in the same conditions, are composed of crystallites with different  
8 sizes and shapes as observed on Figure S3. UiO-66 crystals present a typical octahedral shape with  
9 an average diameter of 220 nm, while UiO-66\_NH<sub>2</sub> crystals are smaller (78 nm) and less faceted.  
10 The packing density of a material is a function of the particles size distribution and their average  
11 size, and their shape.<sup>41</sup> Thus, UiO-66\_NH<sub>2</sub>-based solids might exhibit higher packing densities,  
12 which in turn would allow reaching higher volumetric uptakes and compressive strength. UiO-  
13 66@chitosan and UiO-66\_NH<sub>2</sub>@chitosan extrudates present averaged bulk densities of 0.87 and  
14 0.86 g/cm<sup>3</sup>, respectively. These values are close to the reported 0.79 g/cm<sup>3</sup> reported for MI-101(Cr)  
15 extrudates, and higher than UiO-66 and UiO-66\_NH<sub>2</sub> solids made by granulation (0.67 and 0.56  
16 g/cm<sup>3</sup>, respectively).<sup>35,42</sup> Hence, the bulk density of extrudates is rather dictated by the extrusion

1 process parameters including the inlet flowrate, the die pressure, the screw speed and the torque.<sup>43</sup>  
2 On the contrary, the crystallites size and shape do not seem to have a marked effect on the materials  
3 bulk density.



4  
5 **Figure 2.** SEM micrographs of extrudates made with (a) UiO-66@HEC, (b) UiO-66@chitosan,  
6 (c) UiO-66\_NH<sub>2</sub>@HEC, and (d) UiO-66\_NH<sub>2</sub>@chitosan. Scale bars = (a, b) 1 μm and (c, d) 100  
7 nm.

8 Figures 2 and S4 represent SEM micrographs of extrudates and granules prepared from  
9 UiO-66 and UiO-66\_NH<sub>2</sub> powders, respectively. All solids present a dense packing of MOF  
10 crystallites, and no difference can be observed between extrudates and granules, revealing that the  
11 spheronization process has no impact at the microscopic scale. However, in the case of UiO-66,  
12 significant differences are observed depending on the nature of the binder. When the HEC gel is  
13 used, rounded instead of faceted crystals are observed. This could be due to the binder  
14 preferentially covering the crystals facets. More intriguingly, the use of the chitosan gel results in  
15 the formation of ill-defined and partially agglomerated particles. Individual UiO-66 crystals can  
16 still be observed, but most crystals seem to be incorporated within these bigger particles. In the

1 case of UiO-66\_NH<sub>2</sub>-based solids, however, the crystals retained their shape and size and the  
2 binders presence cannot be observed.

3 The surface and cross-section of representative extrudates and granules were also observed  
4 by SEM and displayed on Figures S5 (UiO-66@chitosan) and S6 (UiO-66\_NH<sub>2</sub>@HEC), arbitrary  
5 chosen as representative solids. Linear microgrooves can be observed over the smooth extrudates  
6 surface (Figures S5.a and S6.a), and are due to the high pressure exerted within the die holes. On  
7 the other hand, the surface of the granules (Figures S5.c and S6.c) is highly fractured and rough,  
8 due to the strong attrition exerted during spheronization. In both cases, the solids are  
9 homogeneously dense over their cross-section.

10 Thermogravimetric curves of the MOF@binder extrudate series (MOF = UiO-66 and UiO-  
11 66\_NH<sub>2</sub> ; binder = HEC or chitosan), displayed on Figure S7, were obtained under air and  
12 compared to their powder counterparts. The first weight loss, below 150 °C, is typically due to the  
13 desorption of weakly physisorbed water molecules. A second weight loss, between 150 °C and  
14 350 °C, corresponds to the deshydroxylation of the MOF as well as possible remaining DMF  
15 entrapped within the porosity,<sup>44</sup> and the combustion of organic binders. As the organic binders  
16 (HEC and chitosan) are thermally decomposed from 250 °C, the solids present lower thermal  
17 stabilities than their MOF powder counterparts. It remains significantly above 140 °C, which is  
18 the typical temperature reached inside FCVS.<sup>8</sup> Also, as the BDC\_NH<sub>2</sub> organic linker starts  
19 degrading from around 300 °C, it is not possible to clearly evaluate its weight loss under these  
20 conditions. Importantly, by subtracting the varying amount of weakly physisorbed water, it is  
21 possible to roughly estimate the binder content in the extrudates, reported in Table 1. The  
22 provisional 3 wt% content is mostly respected for most extrudates (2.4 - 4.2 wt%), excepted for  
23 UiO-66\_NH<sub>2</sub>@HEC which is lower than expected (1.5 wt%). It is noticed that a lower binder



1 content should improve the textural properties of the final material but it will also induce lower  
2 mechanical resistance.

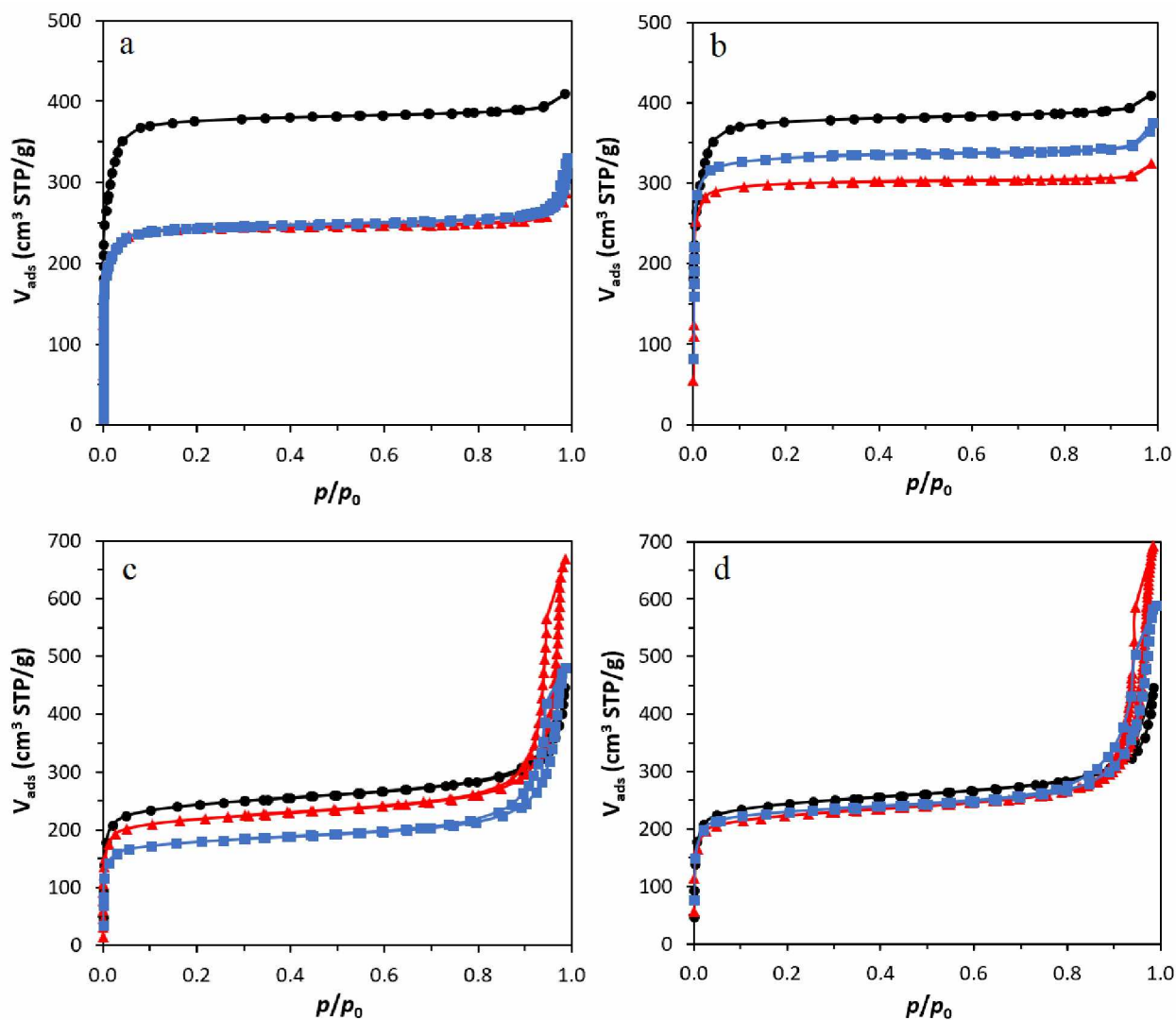
3 The powder X-ray diffractograms of the MOF@binder extrudate and granule series are  
4 given on Figure S8. All solids exhibit a PXRD pattern with well-defined Bragg peaks, and hence  
5 a crystalline structure, matching with the initial UiO-66 or UiO-66\_NH<sub>2</sub> powder counterpart. An  
6 additional small hump around 8.7° (2θ) can be observed on the PXRD patterns of UiO-  
7 66@chitosan solids (see insert on Figure S8.b), which can be attributed to the binder. To verify  
8 this hypothesis, the PXRD pattern of the commercial chitosan is displayed on Figure S9.a. A  
9 diffraction peak at 9.5° (2θ), ascribed to the (020) crystallographic plane of chitin,<sup>45</sup> is clearly  
10 observed. Chitosan is obtained from the deacetylation of chitin, the latter remaining as an impurity.  
11 To evaluate the actual content of chitin within the commercial chitosan, its FTIR spectrum was  
12 measured and is shown on Figure S9.b. The deacetylation degree (DD) of the commercial chitosan  
13 is estimated to be 68 %, meaning that the chitin represents more than 1 wt% of the UiO-  
14 66@chitosan solids.<sup>39</sup> This hump is not visible on the UiO-66\_NH<sub>2</sub>@chitosan solids, owing to its  
15 lesser content. Thus, the extrusion and spheronization processes do not affect UiO-66 and UiO-  
16 66\_NH<sub>2</sub> frameworks owing to their high intrinsic mechanical stability.<sup>34</sup>

17 FTIR measurements were conducted in order to evaluate if the extrusion and  
18 spheronization processes affected the initial chemical properties of the UiO-66 and UiO-66\_NH<sub>2</sub>  
19 powders. The resulting spectra of the MOF@binder extrudate and granule series are shown on  
20 Figure S10, and bands assignment can be found elsewhere.<sup>46</sup> Namely, the most characteristic bands  
21 are found at 482 cm<sup>-1</sup> (Zr-μ<sup>3</sup>O symmetric stretching), 663 cm<sup>-1</sup> (C-C-C aromatic ring), 1398 cm<sup>-1</sup>  
22 (O-C-O symmetric stretching), and 1578 cm<sup>-1</sup> (O-C-O asymmetric stretching). Additional bands at

1 1260 and 1386  $\text{cm}^{-1}$  (C-N stretching) are characteristic of UiO-66-NH<sub>2</sub>. They can all be  
2 superimposed with no additional emerging peak or clear differences of relative intensities,  
3 stressing that all solids have comparable chemical properties with their powder counterpart.  
4 Notably, a band at around 1650  $\text{cm}^{-1}$  ( $\nu_{\text{C=O}}$ ) is attributed to the presence of residual DMF. This  
5 band seems more intense in the case of UiO-66-NH<sub>2</sub>-based materials, which correlates with the  
6 larger weight loss observed by TGA.

7 Nitrogen sorption isotherms of the MOF@binder extrudate and granule series are displayed  
8 on Figure 3 and compared to the initial UiO-66 and UiO-66-NH<sub>2</sub> powders. UiO-66-based  
9 materials are purely microporous, as deduced by their type I isotherm and absence of hysteresis.  
10 On the other hand, UiO-66-NH<sub>2</sub>-based materials present a type I isotherm at low partial pressures  
11 ( $p/p_0 < 0.2$ ) and a type IV isotherm at high partial pressures ( $p/p_0 > 0.7$ ), along with a significant  
12 capillary hysteresis loop. This is classically observed in the case of microporous nanocrystals  
13 (crystals size < 100 nm), offering a considerable intercrystalline porosity upon agglomeration. This  
14 intercrystalline porosity seems promoted by the use of binders, leading to two-fold higher  
15 mesopore volumes ( $V_{\text{meso}}$ ) as compared to the initial UiO-66-NH<sub>2</sub> powder. While there is no clear  
16 correlation between the binder nature or content and the resulting mesoporosity generated, the  
17 spheronization process seems to reduce the final mesoporosity by densifying the solids.

18



1  
 2 **Figure 3.** N<sub>2</sub> adsorption-desorption isotherms of (a) UiO-66 and UiO-66@HEC, (b) UiO-66 and  
 3 UiO-66@chitosan, (c) UiO-66\_NH<sub>2</sub> and UiO-66\_NH<sub>2</sub>@HEC, and (d) UiO-66\_NH<sub>2</sub> and UiO-  
 4 66\_NH<sub>2</sub>@chitosan: (black round) initial MOF powder, (red triangle) MOF@binder extrudates,  
 5 and (blue square) MOF@binder granules.

6 As reported in Table 1, lower BET surface areas and pore volumes are observed for the  
 7 extrudates and granules – even when the proportion of organic binder (1.5 – 4.2 wt%) is taken into  
 8 account. Previous studies reported a similar non-proportional decrease, attributed to partial pore

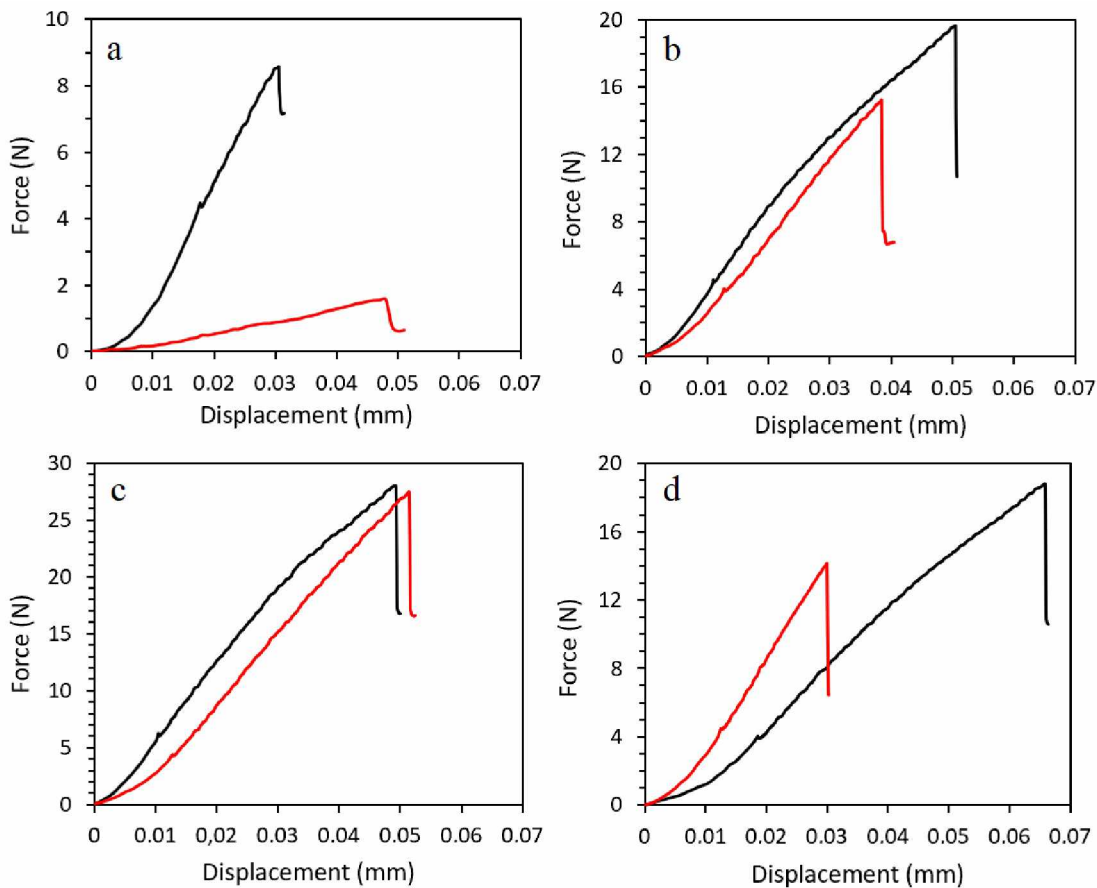
1 blockage by the binders at 77 K.<sup>47</sup> Indeed, the UiO-66\_NH<sub>2</sub>-based solids shaped with less than 2.5  
 2 wt% of binder display a lower BET surface area loss (from -5 to -24 %) than the UiO-66-based  
 3 solids shaped with more than 2.5 wt% of binder (from -15 to -38 %). One may note that, excepted  
 4 in the case of UiO-66\_NH<sub>2</sub>@HEC, all other MOF@binder granules display higher S<sub>BET</sub> values  
 5 than their extrudate counterparts. While it seems counterintuitive, the strong attrition exerted  
 6 during spheronization may free some of the blocked porosity. Thus and as indicated by the  
 7 matching PXRD patterns and FTIR spectra, the shaping processes only have a small influence over  
 8 the physico-chemical properties of the final extrudates and granules including UiO-66 and UiO-  
 9 66\_NH<sub>2</sub>, their impact being more pronounced on UiO-66-based solids, due to the larger content of  
 10 binders, and on extrudates.

11 **Table 1.** Textural properties, average compressive strength ( $\sigma$ ), averaged over 10 samples, and  
 12 estimated binder content (from TGA) of the MOF@binder extrudate and granule series.

Sample	Shape	S <sub>BET</sub> (m <sup>2</sup> /g)	V <sub>μ</sub> (cm <sup>3</sup> /g)	V <sub>meso</sub> (cm <sup>3</sup> /g)	V <sub>meso</sub> (%)	V <sub>tot</sub> (cm <sup>3</sup> /g)	σ (N)	Binder (wt%)
UiO-66	Powder	1510 (100 %)	0.59	0.04	6	0.63	-	-
UiO-66@HEC	Extrudate	941 (62 %)	0.38	0.07	16	0.45	7.23 ± 1.47	2.7
	Granule	1006 (67 %)	0.38	0.13	25	0.51	1.64 ± 0.88	
UiO-66@chitosan	Extrudate	1212 (80 %)	0.47	0.03	6	0.50	19.45 ± 4.68	4.2
	Granule	1291 (85 %)	0.52	0.06	10	0.58	16.88 ± 7.65	
UiO-66_NH <sub>2</sub>	Powder	925 (100 %)	0.39	0.30	43	0.69	-	-
UiO-66_NH <sub>2</sub> @HEC	Extrudate	855 (92 %)	0.35	0.68	66	1.03	14.59 ± 4.62	1.5
	Granule	683 (74 %)	0.28	0.46	62	0.74	11.32 ± 3.25	
UiO-66_NH <sub>2</sub> @chitosan	Extrudate	868 (94 %)	0.35	0.72	67	1.07	13.22 ± 3.81	2.4
	Granule	878 (95 %)	0.36	0.55	60	0.91	8.62 ± 4.10	

13  
 14 The compressive strength of the MOF@binder series was evaluated by crushing each time  
 15 ten extrudates or granules on their edge, and the results are given on Figure 4 and in Table 1. The

1 UiO-66@chitosan, UiO-66\_NH<sub>2</sub>@HEC and UiO-66\_NH<sub>2</sub>@chitosan extrudates and granules all  
2 present high compressive strength, with values exceeding 12 N of resistance before failure.  
3 However, the mechanical resistance of UiO-66@HEC extrudates and granules remains  
4 significantly lower than the other solids of the present study, while also having the most important  
5 BET surface area drop. Extrusion requires pastes with appropriate viscous properties to allow  
6 being conveyed along the screw and pushed through the die holes with minimal resistance. Too  
7 much resistance would induce a significant pressure increase which could, in turn, affect the UiO-  
8 66 framework. Hence, an additional experiment using a co-binder - 2 wt% of Ludox HS-40 - was  
9 conducted. Silica colloids have already been used to prepare MOF granules,<sup>48</sup> and would bring  
10 additional plasticizing properties for the extrusion step. Figure S11 presents the relating  
11 characterization of as-prepared UiO-66@HEC-Ludox extrudates and granules. A clear  
12 improvement of the compressive resistance is reached (*e.g.* 12.7 vs 7.2 N for the extrudates), along  
13 with better preserved BET surface area (1383 m<sup>2</sup>/g: -8 % compared to the initial UiO-66 powder),  
14 compared to UiO-66-HEC extrudates.



1  
 2 **Figure 4.** Representative force-displacement curves of (a) UiO-66@HEC, (b) UiO-66@chitosan,  
 3 (c) UiO-66\_NH<sub>2</sub>@HEC, and (d) UiO-66\_NH<sub>2</sub>@chitosan: (black line) extrudates and (red line)  
 4 granules.

5 Hence, following extrusion and spheronization, highly robust and porous extrudates and  
 6 granules were prepared. For comparison, following wet granulation, binderless granules made  
 7 from UiO-66\_NH<sub>2</sub> were observed with a resistance value of 0.3 N,<sup>8</sup> and UiO-66 granules formed  
 8 with 5 wt% of mesoporous  $\rho$ -alumina binder displayed an average crushing strength of 4.7 N and  
 9 a decrease of  $S_{BET}$  (-13 %) in the range of the decreases reported herein.<sup>35</sup> A considerable  
 10 improvement of the mechanical stability was thus obtained following this novel protocol, related  
 11 to the presence of appropriate binders and the high bulk densities reached. Moreover, the shaping

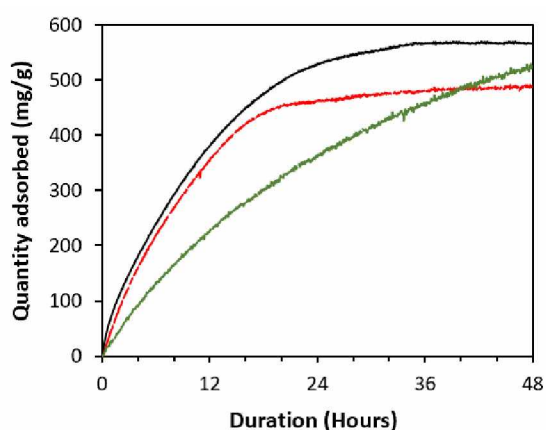
1 protocol developed herein preserved most of the physico-chemical properties of the initial UiO-66  
2 and UiO-66\_NH<sub>2</sub> powders, and especially high BET surface area which is a strong requirement  
3 for most applications involving porous MOF materials, especially for gas sorption. In particular,  
4 owing to its high retained S<sub>BET</sub> along with the additional amino functions brought by the chitosan  
5 binder, UiO-66\_NH<sub>2</sub>@chitosan should be performant for the capture of gaseous iodine.

## 6 **Application of UiO-66 and UiO-66\_NH<sub>2</sub>-based granules for I<sub>2</sub> capture**

7 As a first hint of their potential for the remediation of radioactive iodine, the MOF@binder  
8 granule series were used in a fixed bed setup and submitted to a constant flow of gaseous iodine  
9 at room temperature. The corresponding adsorption kinetic curves are shown on Figure 5 and  
10 Figure S12. As reported elsewhere, the UiO-66\_NH<sub>2</sub>-based materials present superior iodine  
11 adsorption capacity (565 VS 211 mg/g). Recently, the combination of experimentation and DFT  
12 calculations have shown the preferential interaction of molecular iodine with lone electron pair  
13 groups, including amino groups.<sup>12</sup> Of note, I<sub>2</sub> undergoes a kinetic conversion into anionic I<sub>3</sub><sup>-</sup> within  
14 the zirconium-based UiO-n MOFs, which is then slowly desorbed overtime, thus highlighting that  
15 I<sub>2</sub> sorption is mostly governed by physisorption phenomena.<sup>12</sup>

16 Excepted UiO-66\_NH<sub>2</sub>@chitosan, all other MOF-based granules of the series reached their  
17 maximal uptake, characterized by a plateau, before 48 hours. Intuitively, granules are expected to  
18 show greater diffusion restrictions as the MOF crystallites at the core of the granules would be  
19 harder to reach by iodine. Moreover, the latter might flow in-between the granules bed, even if  
20 rapid colour change occurs (from white to purple) for all granules due to the effective capture of  
21 iodine within the pores of the MOFs (Figure S13), while the powder beds are denser in comparison.  
22 For practical comparisons between the materials, a simple analytic equation derived from the

1 Linear Driving Force (LDF) model has been used to the kinetic curves.<sup>49</sup> This approach has been  
2 successfully applied to the study of adsorption kinetics of gaseous species in MOF materials.<sup>50,51</sup>  
3 The fitted and experimental curves can be observed on Figure S14. Of note, as the UiO-66 powder  
4 presents a second small but consistent uptake of iodine (measurement done twice), the resulting  
5 fitting is mediocre. This feature does not appear on the UiO-66-based shaped materials and could  
6 be related to different fluid dynamics within the adsorbent bed.



7  
8 **Figure 5.** Iodine adsorption kinetic curves of UiO-66\_NH<sub>2</sub>-based materials: (black line) UiO-  
9 66\_NH<sub>2</sub> powder, (red line) UiO-66\_NH<sub>2</sub>@HEC granules, and (green line) UiO-66\_NH<sub>2</sub>@chitosan  
10 granules.

11 Table 2 summarizes the iodine adsorption capacity of the MOF@binder granule series and  
12 their powder counterparts, as well as the kinetic constants data. Especially, the granules present an  
13 adsorption capacity that is well correlated with the evolution of their BET surface area after  
14 extrusion and spheronization, as illustrated on Figure S15. This indicates that the amino groups of  
15 chitosan, as well as the hydroxy groups of both HEC and chitosan, have a neglectable role over  
16 the total adsorption capacity toward molecular iodine, and further increasing their content would  
17 reduce the capacity of the materials. Of note, besides the presence of amino moieties in the UiO-



1 66\_NH<sub>2</sub> compound, the presence of chitosan also strongly reduces the mass transfer coefficient  
 2  $k_{LDF}$ , which is even more marked with UiO-66\_NH<sub>2</sub> MOF. It is hypothesized that the amino groups  
 3 of chitosan, located at the surface of the MOF crystals, weakly physisorb some of the molecular  
 4 iodine before releasing it back in the stream. According to the fit, its expected total I<sub>2</sub> adsorption  
 5 capacity should be about 600 mg/g. Also, and as expected, the intercrystalline porosity deduced  
 6 from N<sub>2</sub> isotherms does not seem to contribute to iodine encapsulation within the granules.  
 7 Importantly, the prepared UiO-66\_NH<sub>2</sub>-based granules present I<sub>2</sub> adsorption capacities higher than  
 8 455 mg/g, which is the maximal capacity of silver-doped faujasite zeolites.<sup>5</sup> These granules are  
 9 thus good candidates for further tests under realistic nuclear accidental conditions.

10 **Table 2.** Quantity of iodine captured by UiO-66- and UiO-66\_NH<sub>2</sub>-based materials in relation to  
 11 their BET surface area, and their related kinetic constants data.

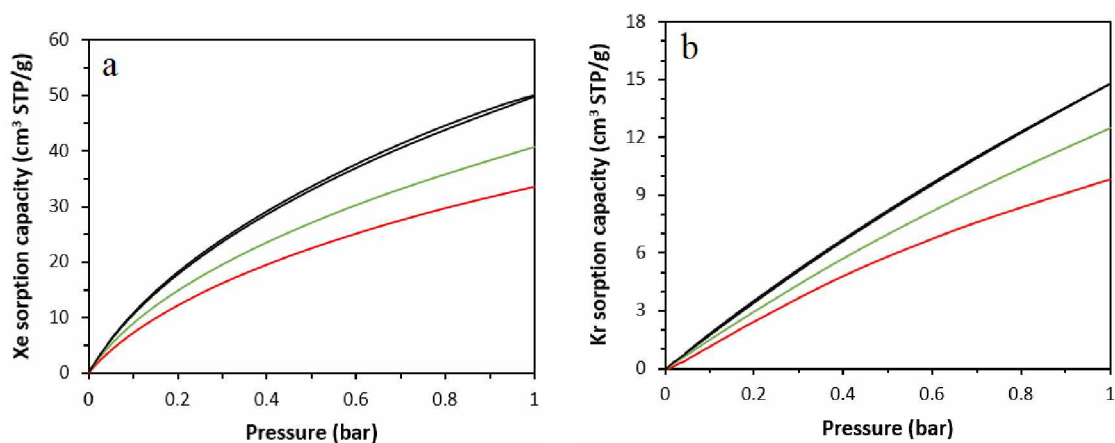
Sample	S <sub>BET</sub> (m <sup>2</sup> /g)	S <sub>BET</sub> (%/powder)	I <sub>2(ads)</sub> (mg/g)	I <sub>2(ads)</sub> (%/powder)	k <sub>LDF</sub> (h <sup>-1</sup> ) <sup>a</sup>	R <sup>2</sup>	t (F = 0.9) (h) <sup>b</sup>
UiO-66	1387	100	211	100	0.170	0.822	13.5
UiO-66@HEC	1006	67	148	66	0.224	0.979	10.3
UiO-66@chitosan	1291	85	190	84	0.151	0.943	15.2
UiO-66_NH <sub>2</sub>	825	100	565	100	0.095	0.992	24.2
UiO-66_NH <sub>2</sub> @HEC	683	83	481	85	0.111	0.994	20.7
UiO-66_NH <sub>2</sub> @chitosan	878	106	527	93 <sup>c</sup>	0.040	0.994	57.6

12 <sup>a</sup> Mass transfer coefficient from the Linear Drive Force (LDF) model:  $F(t) = 1 - \exp[-k_{LDF}t]$ ,  
 13 where F(t) is the fractional uptake. <sup>b</sup> Equilibration time t to reach 90 % of the total adsorption  
 14 capacity, from LDF fit. <sup>c</sup> Plateau not reached after 48 hours.

## 16 Application of UiO-66 and UiO-66\_NH<sub>2</sub>-based granules for Xe/Kr adsorption

17 As a proof of the MOF composites versatility for the nuclear energy field, the granules  
 18 were also used for the adsorption of xenon and krypton gases. According to a computational study  
 19 made by Sikora *et al.*, ideal MOF structures for Xe/Kr separation should present pore diameters

1 from 4.1 Å – slightly larger than an atom of xenon ( $Xe_{\text{kinetic diameter}} = 3.96 \text{ \AA}$ ) – to 8.2 Å, hence  
2 favoring the creation of an induced dipole between the electronic cloud of the gas and the MOF  
3 frameworks, while the cavities should be small enough to hold only one xenon atom.<sup>52</sup> The size of  
4 krypton atoms being smaller ( $Kr_{\text{kinetic diameter}} = 3.60 \text{ \AA}$ ), this gas would have less interactions. With  
5 tetrahedral cages of 7.5 Å and octahedral cages of 12 Å, connected through triangular windows of  
6 about 6 Å, the UiO-66 structure is a good candidate for xenon preferential capture over krypton.



7  
8 **Figure 6.** (a) Xenon and (b) krypton adsorption isotherms of UiO-66-based materials: (black) as-  
9 made powder, (red) UiO-66@HEC granules, and (green) UiO-66@chitosan granules.

10 By exploiting the xenon and krypton isotherms at room temperature, displayed on Figure  
11 6 and Figure S16, it is possible to estimate the MOF composites xenon uptake and Xe/Kr  
12 selectivity. As expected, the adsorption capacity of the materials toward xenon and krypton is  
13 mostly dependent on their BET surface area,<sup>15</sup> with the best performing granular material here  
14 being the UiO-66@chitosan ( $S_{\text{BET}} = 1291 \text{ m}^2/\text{g}$ ). Moreover, both UiO-66\_NH<sub>2</sub>-based granules  
15 show lower Xe and Kr uptakes correlated to their lower BET surface area, implying that the amino  
16 functions do not provide interactions with the noble gases. Lee *et al.* reported higher Xenon  
17 adsorption capacity on UiO-66\_NH<sub>2</sub> (2.3 mmol/g) compared to UiO-66 (1.3 mmol/g), attributed

1 to the ability of amino groups to polarize Xenon preferentially.<sup>53</sup> This observation is not supported  
 2 herein, as the Figure S17 further highlights the linear relationship between the BET surface area  
 3 and the adsorption capacity of the MOF-based materials. Table 3 summarizes the uptake capacity  
 4 of the materials issued from the isotherms as well as the corresponding Xe/Kr adsorption  
 5 selectivity, obtained from the ratio of Henry's constants. The as-made UiO-66 powder exhibit a  
 6 predicted Xe/Kr selectivity of 7.0, in line with the literature (7.2).<sup>53</sup> Importantly, the binders  
 7 presence seems to improve this selectivity, with performances of the UiO-66-based granules (8.1  
 8 to 9.0) higher than their powder counterpart. For comparison, a leading MOF-based material for  
 9 Xe/Kr separation is the HKUST-1 compound, displaying a predicted Xe/Kr selectivity of 8.4 in  
 10 the same conditions.<sup>7</sup> However, its structure is far less stable overtime. This improvement may be  
 11 attributed to a reduction of the flexibility of the MOF frameworks by the binders, especially at low  
 12 pressures (in a range where Henry's constants are calculated),<sup>54</sup> or to partial pore blockage, thus  
 13 reducing the interactions with Kr molecules. Hence, the use of binders could be a good strategy to  
 14 orientate the separation selectivity of MOFs.

15 **Table 3.** Xenon and krypton uptake capacity of UiO-66- and UiO-66\_NH<sub>2</sub>-based materials at 1  
 16 bar and 293.15 K, and the relative Xe/Kr selectivity predicted from the ratio of Henry's constants.

Sample	S <sub>BET</sub> (m <sup>2</sup> /g)	Xe <sub>(ads)</sub> (mmol/g)	Kr <sub>(ads)</sub> (mmol/g)	Xe/Kr selectivity
UiO-66	1510	2.01	0.66	7.0
UiO-66@HEC	1006	1.50	0.38	9.0
UiO-66@chitosan	1291	1.63	0.48	8.1
UiO-66_NH <sub>2</sub>	925	1.35	0.35	7.7
UiO-66_NH <sub>2</sub> @HEC	683	1.20	0.34	7.1
UiO-66_NH <sub>2</sub> @chitosan	878	1.26	0.32	8.3

17

18

## 1 CONCLUSION

2 For the first time, an extrusion-spheronization process has been applied to MOF materials,  
3 namely UiO-66 and UiO-66\_NH<sub>2</sub>. To ensure sufficient robustness of the final objects, up to 6 wt%  
4 of a biosourced binder, either chitosan or 2-hydroxymethyl cellulose (HEC), has been added. The  
5 obtained extrudates and granules present similar physico-chemical properties to the initial UiO-66  
6 and UiO-66\_NH<sub>2</sub> powders, therefore implying that this process is suited for the shaping of MOFs  
7 from the UiO-66 family, and could be applied more broadly to other MOF structures. We pointed  
8 out that the presence of a binder lowers the BET surface area in a non-linear fashion (5-38 % of  
9 S<sub>BET</sub> reduction for 2.0-5.6 wt% of binder), as typically observed, but it also favors the generation  
10 of intercrystalline pores when the crystallites are small enough – in this case with UiO-66\_NH<sub>2</sub>.  
11 Importantly, the as-produced extrudates and granules present a significant mechanical resistance  
12 toward compression, in the range of 7 to 20 N. When an insufficient mechanical resistance is  
13 achieved, as in the case of UiO-66 with 5.0 wt% of HEC, the addition of a co-binder, a colloidal  
14 silica, further improves it (from 7.2 to 12.7 N) while lowering the impact of the process over the  
15 BET surface area (from -38 % to -8 % of S<sub>BET</sub> as compared to the initial powder) by acting as a  
16 plasticizer.

17 The series of shaped UiO-66 and UiO-66\_NH<sub>2</sub>-based granules were further applied to the  
18 capture of iodine. UiO-66\_NH<sub>2</sub>-based granules reached the highest iodine uptake, above 480 mg/g  
19 after 48 hours independently of the binder used. This is in line with the commercial adsorbent used  
20 nowadays (silver-doped faujasite zeolite, 455 mg/g). Finally, these granules were also utilized for  
21 the adsorption of xenon and krypton, with gas uptakes mostly correlated to their BET surface area.  
22 Hence, the UiO-66-based granules presented the highest uptakes, while the predicted Xe/Kr uptake

1 ratio (7.1 to 9.0) was similar for all materials. At last, it was observed that the binders presence  
2 might slightly improve the Xe/Kr selectivity.

3 Hence, the produced MOF-based granules retained most of the performance of the initial  
4 MOF UiO-66 and UiO-66\_NH<sub>2</sub> powders. Their use in a demonstrator under realistic conditions  
5 would be of interest, in particular to evaluate the impact of the binders presence over the long-term  
6 stability of the shaped materials. Also, the broader application of this shaping technique to other  
7 attracting MOF structures is envisaged.

## 1 **ASSOCIATED CONTENT**

2 **Supporting Information.** The Supporting Information is available free of charge on the ACS  
3 Publications website at DOI: .

4 Additional experimental details; photographs of extrusion process and iodine capture test; SEM  
5 micrographs of MOF powders, extrudates, and granules; TGA thermographs, FTIR spectra, N<sub>2</sub>  
6 adsorption-desorption isotherms, PXRD patterns, and representative force-displacement curves for  
7 all materials; iodine adsorption curves for UiO-66-based materials; fitted iodine adsorption kinetic  
8 curves; Xenon and Krypton adsorption-desorption isotherms for UiO-66-NH<sub>2</sub>-based materials;  
9 and correlation curves between the BET surface area and the performance of all materials. The  
10 following files are available free of charge.

## 11 **AUTHOR INFORMATION**

### 12 **Corresponding Author**

13 \*Mail: [jeremy.dhainaut@univ-lille.fr](mailto:jeremy.dhainaut@univ-lille.fr).

### 14 **Author Contributions**

15 J.D, T.L. and C.V. conceived and designed the project. S.R. and J.D. acquired the funding. J.D.  
16 prepared the MOF powders. A.A. shaped the materials. A.A and J.D. conducted all  
17 characterizations. M.L., N.C. and J.D. measured I<sub>2</sub> adsorption. N.C. measured Kr and Xe  
18 isotherms. A.A. and J.D. analyzed the data. J.D. wrote the manuscript. All authors discussed the  
19 results and commented on the manuscript.

## 20 **ACKNOWLEDGMENT**

1 The CNRS, the Chevreul Institute (FR 2638), the Ministère de l'Enseignement Supérieur et de la  
2 Recherche, the Région Hauts-de-France and the FEDER are acknowledged for supporting this  
3 work. M.L. acknowledges the French Institut de Radioprotection et de Sûreté Nucléaire (IRSN)  
4 and Région Hauts-de-France for her PhD grant funding. N.C. acknowledges ANR ASTRID project  
5 TEXMOF for her post-doc grant funding.

## 6 REFERENCES

- 7 (1) Bal, M.; Jose, R.C.; Meikap, B.C. Control of Accidental Discharge of Radioactive Materials  
8 by Filtered Containment Venting System: A Review. *Nucl. Eng. Technol.* **2019**, *51*, 931-942.
- 9 (2) Mathieu, A.; Kajino, M.; Korsakissok, I.; Périllat, R.; Quélo, D.; Quérel, A.; Saunier, O.;  
10 Sekiyama, T.T.; Igarashi, Y.; Didier, D. Fukushima Daiichi-Derived Radionuclides in the  
11 Atmosphere, Transport and Deposition in Japan : A Review. *Appl. Geochem.* **2018**, *91*, 122-139.
- 12 (3) Tronko, M.D.; Howe, G.R.; Bogdanova, T.I.; Bouville, A.C.; Epstein, O.V.; Brill, A.B.;  
13 Likhtarev, I.A.; Fink, D.J.; Markov, V.V.; Greenebaum, E.; Olijnyk, V.A.; Masnyk, I.J.; Shpak,  
14 V.M.; McConnell, R.J.; Tereshchenko, V.P.; Robbins, J.; Zvinchuk, O.V.; Zablotska, L.B.; Hatch,  
15 M.; Luckyanov, N.K.; Ron, E.; Thomas, T.L.; Voillequé, P.G.; Beebe, G.W. A Cohort Study of  
16 Thyroid Cancer and Other Thyroid Diseases After the Chernobyl Accident: Thyroid Cancer in  
17 Ukraine Detected During First Screening. *J. Natl. Cancer Inst.* **2006**, *98*, 897-903.
- 18 (4) Leroy, O.; Monsanglant-Louvet, C. Trapping Measurements of Volatile Iodine by Sand Bed  
19 and Metallic Filters. *J. Radioanalytical Nucl. Chem.* **2019**, *322*, 913-922.
- 20 (5) Azambre, B.; Chebbi, M.; Leroy, O.; Cantrel, L. Effects of Zeolitic Parameters and Irradiation  
21 on the Retention Properties of Silver Zeolites Exposed to Molecular Iodine. *Ind. Eng. Chem. Res.*  
22 **2018**, *57*, 1468-1479.
- 23 (6) Chebbi, M.; Chibani, S.; Paul, J.-F.; Cantrel, L.; Badawi, M. Evaluation of Volatile Iodine

1 Trapping in Presence of Contaminants: A Periodic DFT Study on Cation-Exchanged-Faujasite.  
2 *Micro. Meso. Mater.* **2017**, *239*, 111-122.

3 (7) Huve, J.; Ryzhikov, A.; Nouali, H.; Lalia, V.; Augé, G.; Daou, T.J. Porous Sorbents for the  
4 Capture of Radioactive Iodine Compounds: A Review. *RSC Adv.* **2018**, *8*, 29258-29273.

5 (8) Leloire, M.; Dhainaut, J.; Devaux, P.; Leroy, O.; Desjonqueres, H.; Poirier, S.; Nerisson, P.;  
6 Cantrel, L.; Royer, S.; Loiseau, T.; Volkringer, C. Stability and Radioactive Gaseous Iodine-131  
7 Retention Capacity of Binderless UiO-66\_NH<sub>2</sub> Granules Under Severe Nuclear Accidental  
8 Conditions. *J. Hazard. Mater.* **2021**, *416*, 125890.

9 (9) Lee, H.C.; Lee, D.Y.; Kim, H.S.; Kim, C.R. Performance Evaluation of TEDA Impregnated  
10 Activated Carbon under Long Term Operation Simulated NPP Operating Conditions. *Nucl. Eng.*  
11 *Technol.* **2020**, *52*, 2652-2659.

12 (10) Sava, D.F.; Rodriguez, M.A.; Chapman, K.W.; Chupas, P.J.; Greathouse, J.A.; Crozier, P.S.;  
13 Nenoff, T.M. Capture of Volatile Iodine, a Gaseous Fission Product, by Zeolitic Imidazolate  
14 Framework-8. *J. Am. Chem. Soc.* **2011**, *133*, 12398-12401.

15 (11) Falaise, C.; Volkringer, C.; Facqueur, J.; Bousquet, T.; Gasnot, L.; Loiseau, T. Capture of  
16 Iodine in Highly Stable Metal-Organic Frameworks: A Systematic Study. *Chem. Commun.* **2013**,  
17 *49*, 10320-10322.

18 (12) Leloire, M.; Walshe, C.; Devaux, P.; Giovine, R.; Duval, S.; Bousquet, T.; Chibani, S.; Paul,  
19 J.-P.; Moissette, A.; Vezin, H.; Nerisson, P.; Cantrel, L.; Volkringer, C.; Loiseau, C. Capture of  
20 Gaseous Iodine in Isorecticular Zirconium-based UiO-n Metal-Organic Frameworks : Influence of  
21 Amino Functionalization, DFT Calculations, Raman and EPR Spectroscopic Investigations.  
22 *Chem. Eur. J.* **2022** (Just Accepted). DOI: 10.1002/chem.202104437.

23



- 1 (13) Marshall, R.J.; Griffin, S.L.; Wilson, C.; Forgan, R.S. Stereoselective Halogenation of  
2 Integral Unsaturated C-C bonds in Chemically and Mechanically Robust Zr and Hf MOFs. *Chem.*  
3 *Eur. J.* **2016**, *22*, 4870-4877.
- 4 (14) Jelea, A. An Equation of State for Xenon/Krypton Mixtures Confined in the Nuclear Fuels.  
5 *J. Nucl. Mater.* **2020**, *530*, 151952.
- 6 (15) Banerjee, D.; Simon, C.M.; Elsaidi, S.K.; Haranczyk, M.; Thallapally, P.K. Xenon Gas  
7 Separation and Storage Using Metal-Organic Frameworks. *Chem* **2018**, *4*, 466-494.
- 8 (16) Thallapally, P.K.; Grate, J.W.; Motkuri, R.K. Facile Xenon Capture and Release at Room  
9 Temperature using a Metal-Organic Framework: A Comparison with Activated Charcoal. *Chem.*  
10 *Commun.* **2012**, *48*, 347-349.
- 11 (17) Jameson, C.J.; Jameson, A.K.; Lim, H.M. Competitive Adsorption of Xenon and Krypton in  
12 Zeolite NaA: Xe-129 Nuclear Magnetic Resonance Studies and Grand Canonical Monte Carlo  
13 Simulations. *J. Chem. Phys.* **1997**, *107*, 4364-4372.
- 14 (18) Daniel, C.; Elbaraoui, A. Aguado, S.; Springuel-Huet, M.A.; Nossov, A.; Fontaine, J.P.;  
15 Topin, S.; Taffary, T.; Deliere, L.; Schuurman, Y.; Farrusseng, D. Xenon Capture on Silver-  
16 Loaded Zeolites: Characterization of Very Strong Adsorption Sites. *J. Phys. Chem. C* **2013**, *117*,  
17 15122-15129.
- 18 (19) Banerjee, D.; Simon, C.M.; Plonka, A.M.; Motkuri, R.K.; Liu, J.; Chen, X.; Smit, B.; Parise,  
19 J.B.; Haranczyk, M.; Thallapally, P.K. Metal-Organic Framework with Optimally Selective Xenon  
20 Adsorption and Separation. *Nat. Commun.* **2016**, *7*, 11831.
- 21 (20) Perry, J.J. IV; Teich-McGoldrick, S.L.; Meek, S.T.; Greathouse, J.A.; Haranczyk, M.;  
22 Allendorf, M.D. Noble Gas Adsorption in Metal-Organic Frameworks Containing Open Metal  
23 Sites. *J. Phys. Chem. C* **2014**, *118*, 11685-11698.

- 1 (21) Mueller, U.; Schubert, M.; Teich, F.; Puetter, H.; Schierle-Arndt, K.; Pastré, J. Metal-Organic  
2 Frameworks-Prospective Industrial Applications. *J. Mater. Chem.* **2006**, *16*, 626-636.
- 3 (22) Howarth, A.J.; Liu, Y.; Li, P.; Li, Z.; Wang, T.C.; Hupp, J.T.; Farha, O.K. Chemical, Thermal  
4 and Mechanical Stabilities of Metal-Organic Frameworks. *Nat. Rev.* **2016**, *1*, 15018.
- 5 (23) Cavka, J.H.; Jakobsen, S.; Olsbye, U.; Guillou, N.; Lamberti, C.; Bordiga, S.; Lillerud, K.P.  
6 A New Zirconium Inorganic Building Brick Forming Metal Organic Frameworks with Exceptional  
7 Stability, *J. Am. Chem. Soc.* **2008**, *130*, 13850-13851.
- 8 (24) Chen, Z.; Hanna, S.L.; Redfern, L.R.; Alezi, D.; Islamoglu, T.; Farha, O.K. Reticular  
9 Chemistry in the Rational Synthesis of Functional Zirconium Cluster-based MOFs. *Coord. Chem.*  
10 *Rev.* **2019**, *386*, 32-49.
- 11 (25) Falaise, C.; Volkringer, C.; Vigier, J.-F.; Henry, N.; Beaurain, A.; Loiseau, T. Three-  
12 Dimensional MOF-Type Architectures with Tetravalent Uranium Hexanuclear Motifs (U<sub>6</sub>O<sub>8</sub>).  
13 *Chem. Eur. J.* **2013**, *19*, 5324-5331.
- 14 (26) Falaise, C.; Charles, J.-S.; Volkringer, C.; Loiseau, T. Thorium Terephthalates Coordination  
15 Polymers Synthesized in Solvothermal DMF/H<sub>2</sub>O System. *Inorg. Chem.* **2015**, *54*, 2235-2242.
- 16 (27) Martin, N.P.; März, J.; Feuchter, H.; Duval, S.; Roussel, P.; Henry, N.; Ikeda-Ohno, A.;  
17 Loiseau, T.; Volkringer, C. Synthesis and Structural Characterization of the First Neptunium based  
18 Metal-Organic Frameworks Incorporating {Np<sub>6</sub>O<sub>8</sub>} Hexanuclear Clusters. *Chem. Commun.* **2018**,  
19 *54*, 6979-6982.
- 20 (28) Bai, Y.; Dou, Y.; Xie, L.-H.; Rutledge, W.; Li, J.-R.; Zhou, H.-C. Zr-based Metal-Organic  
21 Frameworks: Design, Synthesis, Structure, and Applications. *Chem. Soc. Rev.* **2016**, *45*, 2327-  
22 2367.
- 23 (29) Xie, W.; Cui, D.; Zhang, S.R.; Xu, Y.H.; Jiang, D.L. Iodine Capture in Porous Organic

1 Polymers and Metal-Organic Frameworks Materials. *Mater. Horiz.* **2019**, *4*, 1571-1595.

2 (30) Peterson, G.W.; Mahle, J.J.; DeCoste, J.B.; Gordon, W.O.; Rossin, J.A. Extraordinary NO<sub>2</sub>  
3 Removal by the Metal-Organic Framework UiO-66\_NH<sub>2</sub>. *Angew. Chem. Int. Ed.* **2016**, *55*, 6235-  
4 6238.

5 (31) Browe, M.A.; Napolitano, A.; DeCoste, J.B.; Peterson, G.W. Filtration of Chlorine and  
6 Hydrogen Chloride Gas by Engineered UiO-66\_NH<sub>2</sub> Metal-Organic Framework. *J. Hazard.*  
7 *Mater.* **2017**, *332*, 162-167.

8 (32) Cmarik, G.E.; Kim, M.; Cohen, S.M.; Walton, K.S. Tuning the Adsorption Properties of UiO-  
9 66 via Ligand Functionalization. *Langmuir* **2012**, *28*, 15606-15613.

10 (33) Yeskendir, B.; Dacquin, J.-P.; Lorgouilloux, Y.; Courtois, C.; Royer, S.; Dhainaut, J. From  
11 Metal-Organic Framework Powders to Shaped Solids: Recent Developments and Challenges.  
12 *Mater. Adv.* **2021**, *2*, 7139-7186.

13 (34) Dhainaut, J.; Avci-Camur, C.; Troyano, J.; Legrand, A.; Canivet, J.; Imaz, I.; Maspoeh, D.;  
14 Reinsch, H.; Farrusseng, D. Systematic Study of the Impact of MOF Densification into Tablets on  
15 Textural and Mechanical Properties. *CrystEngComm* **2017**, *19*, 4211-4218.

16 (35) Valekar, A.H.; Cho, K.-H.; Lee, U.-H.; Lee, J.S.; Yoon, J.W.; Hwang, Y.K.; Lee, S.G.; Cho,  
17 S.J.; Chang, J.-S. Shaping of Porous Metal-Organic Framework Granules using Mesoporous  $\rho$ -  
18 Alumina as a Binder. *RSC Adv.* **2017**, *7*, 55767-55777.

19 (36) Chanut, N.; Wiersum, A.D.; Lee, U.; Hwang, K.; Ragon, F.; Chevreau, H.; Bourrelly, S.;  
20 Kuchta, B.; Chang, J.; Serre, C.; Llewellyn, P.L. Observing the Effects of Shaping on Gas  
21 Adsorption in Metal-Organic Frameworks, *Eur. J. Inorg. Chem.* **2016**, *27*, 4416-4423.

22 (37) Ren, J.; Musyoka, N.M.; Langmi, H.W.; Swartbooi, A.; North, B.C.; Mathe M. A More  
23 Efficient Way to Shape Metal-Organic Framework (MOF) Powder Materials for Hydrogen

- 1 Storage Applications, *Int. J. Hydrog. Energy* **2015**, *40*, 4617–4622.
- 2 (38) Khabzina, Y.; Dhainaut, J.; Ahlhelm, M.; Richter, H.-J.; Reinsch, H.; Stock, N. Farrusseng,  
3 D. Synthesis and Shaping Scale-up Study of Functionalized UiO-66 MOF for Ammonia Air  
4 Purification Filters. *Ind. Eng. Chem. Res.* **2018**, *57*, 8200-8208.
- 5 (39) Brugnerotto, J.; Lizardi, J.; Goycoolea, F.M.; Argüelles-Monal, W.; Desbrières, J.; Rinaudo,  
6 M. An Infrared Investigation in Relation with Chitin and Chitosan Characterization. *Polymer* **2001**,  
7 *42*, 3569-3580.
- 8 (40) Petrovick, G.F.; Breikreutz, J. Spheronization of Solid Lipid Extrudates: Elucidation of  
9 Spheroid Formation Mechanism. *Eur. J. Pharm. Biopharm.* **2018**, *125*, 148-158.
- 10 (41) Sohn, H.Y.; Moreland, C. The Effect of Particle Size Distribution on Packing Density. *Can.*  
11 *J. Chem. Eng.* **1968**, *46*, 162-167.
- 12 (42) Hong, W.Y.; Perera, S.P.; Burrows, A.D. Manufacturing of Metal-Organic Framework  
13 Monoliths and their Application in CO<sub>2</sub> Adsorption. *Micro. Meso. Mater.* **2015**, *214*, 149-155.
- 14 (43) Cheng, H.; Høeg Hansen, J.; Tolderlund Rasmussen, H. A General Extrudate Bulk Density  
15 Model for both Twin-Screw and Single-Screw Extruder Extrusion Cooking Processes. *J. Food.*  
16 *Eng.* **2010**, *78*, 10-19.
- 17 (44) Shearer, G.C.; Forselv, S.; Chavan, S.; Bordiga, S.; Mathisen, K.; Bjørgen, M.; Svelle, S.;  
18 Lillerud, K.P. In Situ Infrared Spectroscopic and Gravimetric Characterisation of the Solvent  
19 Removal and Dehydroxylation of the Metal Organic Frameworks UiO-66 and UiO-67. *Topics*  
20 *Catal.* **2013**, *56*, 770-782.
- 21 (45) Kaya, M.; Mujtaba, M.; Ehrlich, H.; Salaberria, A.M.; Baran, T.; Amemiya, C.T.; Galli, R.;  
22 Akyuz, L.; Sargin, I.; Labidi, J. On Chemistry of  $\gamma$ -Chitin. *Carbohydr. Polym.* **2017**, *176*, 177-186.
- 23 (46) Valenzano, L.; Civalleri, B.; Chavan, S.; Bordiga, S.; Nilsen, M.H.; Jakobsen, S.; Lillerud,

1 K.P.; Lamberti, C. Disclosing the Complex Structure of UiO-66 Metal Organic Framework: A  
2 Synergic Combination of Experiment and Theory. *Chem. Mater.* **2011**, *23*, 1700-1718.

3 (47) Dhainaut, J.; Bonneau, M.; Ueoka, R.; Kanamori, K.; Furukawa, S. Formulation of Metal-  
4 Organic Framework Inks for the 3D Printing of Robust Microporous Solids Toward High-Pressure  
5 Gas Storage and Separation. *ACS Appl. Mater. Interfaces* **2020**, *12*, 10983-10992.

6 (48) Kim, P.; You, Y.; Park, H.; Chang, J.; Bae, Y.; Lee, C.; Suh, J. Separation of SF<sub>6</sub> from SF<sub>6</sub>/N<sub>2</sub>  
7 Mixture using Metal-Organic Framework MIL-100(Fe) Granule. *Chem. Eng. J.* **2015**, *262*, 683-  
8 690.

9 (49) Sircar, S.; Hufton, J.R. Why does the Linear Driving Force Model for Adsorption Kinetics  
10 Work? *Adsorption* **2000**, *6*, 137-147.

11 (50) Blăniță, G.; Streza, M.; Lazăr, M.D.; Lupu, D. Kinetics of Hydrogen Adsorption in MIL-101  
12 Single Pellets. *Int. J. Hydrog. Energy* **2017**, *42*, 3064-3077.

13 (51) Streza, M.; Grad, O.; Lazăr, M.D.; Depriester, M.; Longuemart, S.; Sahraoui, A.H.; Blăniță,  
14 G.; Lupu, D. Hybrid MOFs-Graphene Composites: Correlation Between Thermal Transport and  
15 Kinetics of Hydrogen Adsorption. *Int. J. Heat Mass. Transfer* **2019**, *143*, 118539.

16 (52) Sikora, B.J.; Wilmer, C.E.; Greenfield, M.L.; Snurr, R.Q. Thermodynamic Analysis of Xe/Kr  
17 Selectivity in over 137 000 Hypothetical Metal-Organic Frameworks. *Chem. Sci.* **2012**, *3*, 2217-  
18 2223.

19 (53) Lee, S.-J.; Yoon, T.-U.; Kim, A.-R.; Kim, S.-Y.; Cho, K.-H.; Hwang, Y.K.; Yeon, J.-W.; Bae,  
20 Y.-S. Adsorptive Separation of Xenon/Krypton Mixtures using a Zirconium-based Metal-Organic  
21 Framework with High Hydrothermal and Radioactive Stabilities. *J. Hazardous Mater.* **2016**, *320*,  
22 513-520.

23 (54) Kriesten, M.; Schmitz, J.V.; Siegel, J.; Smith, C.E.; Kaspereit, M.; Hartmann, M. Shaping of

- 1 Flexible Metal-Organic Frameworks: Combining Macroscopic Stability and Framework
- 2 Flexibility. *Eur. J. Inorg. Chem.* **2019**, *43*, 4700-4709.